



# Effect of Welding Parameters on the Liquation Cracking Behavior of High-Chromium Ni-Based Superalloy

Amirhossein Mashhuriazar, Hamid Omidvar, C. Hakan Gur, and Zainuddin Sajuri

Submitted: 28 March 2020 / Revised: 4 October 2020 / Accepted: 17 October 2020 / Published online: 16 November 2020

Gas turbine blades working under extremely harsh operating conditions are made of superalloys. These superalloys are exposed to various damage mechanisms, which wear them out gradually. Welding is often preferred to repair the damaged components for cost minimization. This study aimed to investigate the effects of flexural load, heat input, and welding speed on the weldability and intergranular liquation cracking of high-chromium Ni-based superalloy. For this purpose, a series of Sigma-jig tests designed based on the Taguchi method with L4 array, as well as microstructure investigations and residual stress measurements, were performed. The results showed that the microstructures of heat-affected zones (HAZs) were highly susceptible to cracking during the welding process, and all of these cracks appeared in the HAZ and grew perpendicular to the melting zone along grain boundaries. Flexural load contributed the most substantial impact (82%) on crack propagation compared with the 9.7 and 9.2% impacts of welding speed and welding heat input, respectively. We found that the lowest flexural load, welding speed, and heat input are the best welding parameters to reduce the total crack lengths at the welded area of high-chromium Ni-based superalloy.

**Keywords** flexural load, heat input, Inconel 939, superalloy, welding, welding speed

## 1. Introduction

Gas turbine blades are typically made of superalloys to provide a long service life with a satisfactory performance under high-temperature and high-stress operating conditions (Ref 1-3). High-chromium nickel-based superalloy, Inconel 939 (IN-939) is a popular choice in the manufacturing of the high-temperature components of a gas turbine. IN-939 is a precipitation-hardened Ni-based superalloy with excellent properties, such as high-temperature mechanical properties and high resistance to corrosion and oxidation (Ref 4). Extremely harsh operating conditions damage gas turbine blades through various mechanisms, such as surface erosion (Ref 5), hot corrosion (Ref 6), high-temperature fatigue cracking (Ref 7, 8), oxidation, and sulfidation (Ref 9). The manufacturing of superalloy components is costly and rather difficult; thus, the repair and reassembly of damaged parts might be more practical and cost-effective than replacing them (Ref 10). Moreover, the components have complex geometries, which are impossible to manufacture via casting or forging

processes, as they have to be fabricated in several pieces and then assembled by welding (Ref 11).

Fusion welding has extremely limited use in the production and repair of precipitation-hardened Ni-based superalloys (Ref 12). Ni-based superalloys contain a high volume fraction of  $\gamma'$ , which is the main reinforcing precipitate in the microstructure; thus, the superalloys are very susceptible to micro-cracking during welding, especially in the heat-affected zone (HAZ) (Ref 13). This susceptibility largely depends on the composition and microstructure of the base metal, which can be optimized to attain the properties needed (Ref 14). Such cracks grow along grain boundaries in the HAZ near the weld line (Ref 15). Although the mechanism of cracking is still unclear, many of the studies that attempted to eliminate or minimize cracking in the HAZ of similar superalloys focused on the following factors: carbide precipitation between grains, which reduces the strength of grain boundaries (Ref 16); the precipitation of the  $\gamma'$  phase and the depletion of grain boundaries from Al and Ti (Ref 17); metallurgical changes during welding and the possibility of partial melting (Ref 18); and high stress during welding. The HAZ also has the highest residual stress in a material and very high dislocation density (Ref 17).

Research on IN-939 superalloy is largely concerned with the effect of heat treatment on microstructure (Ref 19) and high-temperature mechanical properties (Ref 20). Some researchers investigated the effect of pre-welding heat treatment on weldability (Ref 15). González et al. studied the effect of pre-welding heat treatment on the microstructure of the HAZ and its effect on the appearance of micro-cracks during the repair welding of IN-939. They reported that pre-welding heat treatment has a substantial impact on the morphology and volume fraction of  $\gamma'$  precipitates. The specimens whose microstructure had primary and secondary spherical  $\gamma'$  precipitates experienced less cracking in their HAZ than those with square  $\gamma'$  precipitates. In another study (Ref 21), the effect of aging temperature on the lattice parameters was investigated, and the degree of mismatch between the crystalline lattice of  $\gamma'$  precipitate and  $\gamma$  substrate

Amirhossein Mashhuriazar and Hamid Omidvar, Department of Materials and Metallurgical Engineering, Amirkabir University of Technology, Tehran 1599637111, Iran; C. Hakan Gur, Department of Metallurgical and Materials Engineering, Middle East Technical University, Ankara 06800, Turkey; and Zainuddin Sajuri, Department of Mechanical and Manufacturing Engineering, Faculty of Engineering and Built Environment, Universiti Kebangsaan Malaysia, 43600 Bangi, Selangor, Malaysia. Contact e-mail: omidvar@aut.ac.ir.

was determined. The initial microstructure of the base metal has an impact on the final microstructure of the HAZ. A lower mismatch between  $\gamma'$  precipitates and substrate results in lower dislocation density, and consequently, lower local strain, which leads to a substantial reduction in crack formation.

Despite the importance and widespread use of welding for the manufacture and repair of components made of IN-939, only a few have reported welding metallurgy, weldability, and the reduction of cracking by adjusting welding parameters (Ref 15, 22). The impact of each welding parameter on crack length and stress generation has not been reported in the literature. Hence, this study aimed to examine the microstructural changes that occur in IN-939 as a result of welding and the effects of welding flexural load, speed, and heat input on the weldability and residual stress generation during welding.

## 2. Experimental

### 2.1 Materials

The master alloy used in this study was obtained from the root of scrapped and damaged gas turbine blades made of IN-

939. The material was then heated to melt in a vacuum induction furnace and cast into square ingots. Casting was performed at a temperature of 1450 °C and a vacuum of  $\sim 10^{-5}$  Torr, and then the temperature was decreased at  $\sim 10$  °C/min cooling rate. The ingots were re-melted in a vacuum furnace in a ceramic mold preheated to  $\sim 800$  °C and superheated at 1400 °C for 5 min. Finally, the ingots were subjected to hot isostatic pressing under 103 MPa pressure at 1185 °C for 4 h. IN-939 specimens with dimensions of 10 mm  $\times$  50 mm  $\times$  100 mm were prepared as shown in Fig. 1(a). The chemical composition of the material was determined by x-ray fluorescence technique, and the result is presented in Table 1. Before the welding procedure, conventional radiographic examination was performed at 170 kV and 0.8 mA with a focal spot size of 2 mm for 1.3 min to evaluate the quality of the products and ensure that the samples used for the study have no initial defects.

### 2.2 Specimen Preparation and Microstructural Examination

All the specimens used in this study were subjected to solution heat treatment for a 4-h heat cycle at 1160 °C at a heating rate of 2 °C/min followed by furnace-cooling (Ref 22) prior to the hot-cracking (Sigmajig) test. The pre-welding heat treatment process was carried out in a vacuum furnace with  $10^{-4}$  Torr pressure. Sigmajig tests were performed to evaluate the effect of welding parameters on the cracking behavior of IN-939. The Sigmajig test fixture and welding torch are shown in Fig. 1(b). The fixture holds the specimen between hardened steel grips and applies a transverse stress before welding. A weldment is produced in the centerline of the specimen after pre-loading using an autogenous gas tungsten arc (GTA). The experiments were conducted according to the welding parameters shown in Table 2. These parameters were selected according to the previous study by González Albarrán et al. on the weldability of IN-939 (Ref 23). The effect of pre-loading was investigated by changing the flexural load, welding speed, and heat input. The heat input energy (in kilojoules per millimeter) of the arc was calculated by using the formula:  $(V \times A \times 60)/(S \times 1000)$ , where  $V$  is the arc voltage,  $A$  is the welding current, and  $S$  is the welding speed or arc travel speed (Ref 15). These parameters are essential in welding and can be varied by changing the current.

Radiographic examination was performed after welding to evaluate the quality of the welds. The samples were ground using emery papers up to grade 2000, polished, and then etched

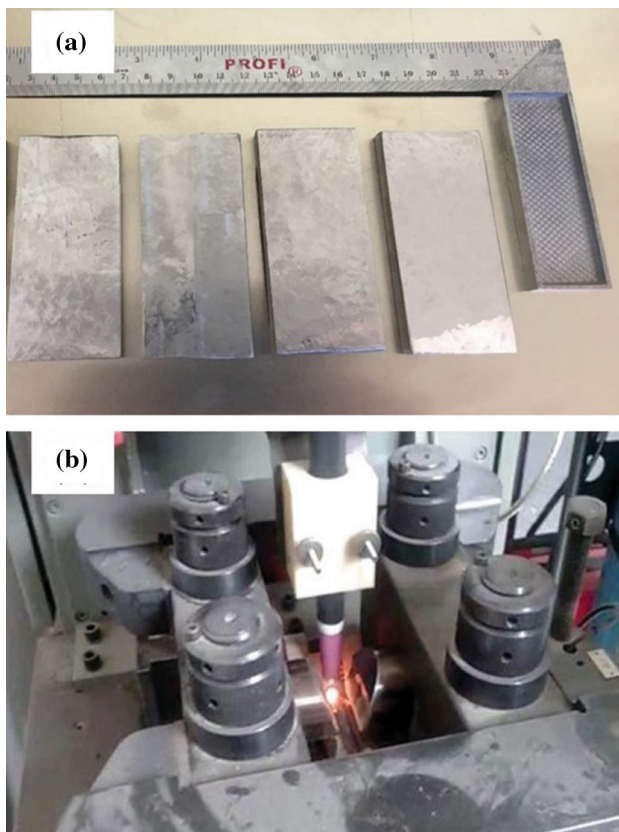


**Fig. 1** Sigmajig test: (a) specimens and (b) experimental set up for GTA welding

**Table 1** Chemical composition of the base metal (wt.%)

Ni	Al	Ti	Mn	B	Nb	Mo	Ta	C	W	Co	Cr
Balance	1.59	3.22	0.02	0.01	0.65	0.24	2.00	0.14	2.53	16.08	27.1

**Table 2** Conditions and order of the Sigmajig test

Sample no.	Flexural load, kN	Heat input, kJ/mm	Travel speed, cm/min
1	2500	2.650	18
2	2500	2.450	20
3	1250	2.650	20
4	1250	2.450	18

with marble (10 g CuSO<sub>4</sub>, 50 ml hydrochloric acid, and 50 ml water) for 7 s. Microstructural examination and quantitative chemical compositional analysis were performed using a light microscope and Tescan Mira3 XMU<sup>®</sup> field emission scanning electron microscope (FESEM) equipped with an ultra-thin window energy dispersive x-ray spectrometer (EDS), working at 15 kV accelerating voltage. The microhardness of the welded areas was also measured by applying a force of 9.2 N and a dwell time of 15 s using a Vickers hardness tester. ImageJ 1.44p<sup>®</sup> software was used to measure the average sizes of different zones and the area fraction of precipitates, the number of cracks, total crack length (TCL), and average crack length (ACL) from five cross-sections.

### 2.3 Residual Stress Examination

The residual stresses of the as-welded specimens were measured by x-ray diffraction (XRD)-sin<sup>2</sup>ψ method according to previous studies (Ref 24-27). Computer-programmed X-Pert X-ray<sup>®</sup> was employed for XRD using a Cr Kα radiation source (λ = 0.2289760 nm for Kα1) working at 40 kV and 30 mA (Model: Philips-PW1730). Scanning was performed in the angular range of 77.99° to 81.50° in steps of 0.03° with a dwell time of 0.80 s at each step to obtain quality data. The values were obtained over an area of 12.0 × 0.4 mm<sup>2</sup>. Finally, the peak shift at various angles (ranging from 0° to 33° in steps of 1.3°) and *d*-spacing relationship were used to estimate the

residual stresses. Finally, the stress was estimated by the *d* – sin<sup>2</sup>ψ diagram of the specimen.

## 3. Results and Discussion

### 3.1 Microstructure of Base Metal

Figure 2 displays the microstructure of the base metal after hot isostatic pressing at 103 MPa and 1185 °C for 4 h. The microstructure of the austenitic base shows clear signs of separation and dendrite morphology (Fig. 2a). The MC carbides that precipitated at the grain boundaries or within the grains are evident in Fig. 2(b). The role of carbides in Ni-based superalloys is very complex (Ref 28). Carbides influence mechanical properties depending on their morphology and distribution. Ti-rich MC carbides in the form of fine blocks are dispersed over the matrix and form discrete particles in intergranular and intragranular positions between the dendrites during solidification. These carbides form in the liquid phase because of the strong segregation of C and usually have coarse cubic or script morphology that react with Ti and Mo when their amount is above 0.05%. Their dense, closely packed face-centered cubic structures contribute to the strength and chemical stability of these compounds. They are stable at low temperatures but tend to degenerate into secondary carbides at

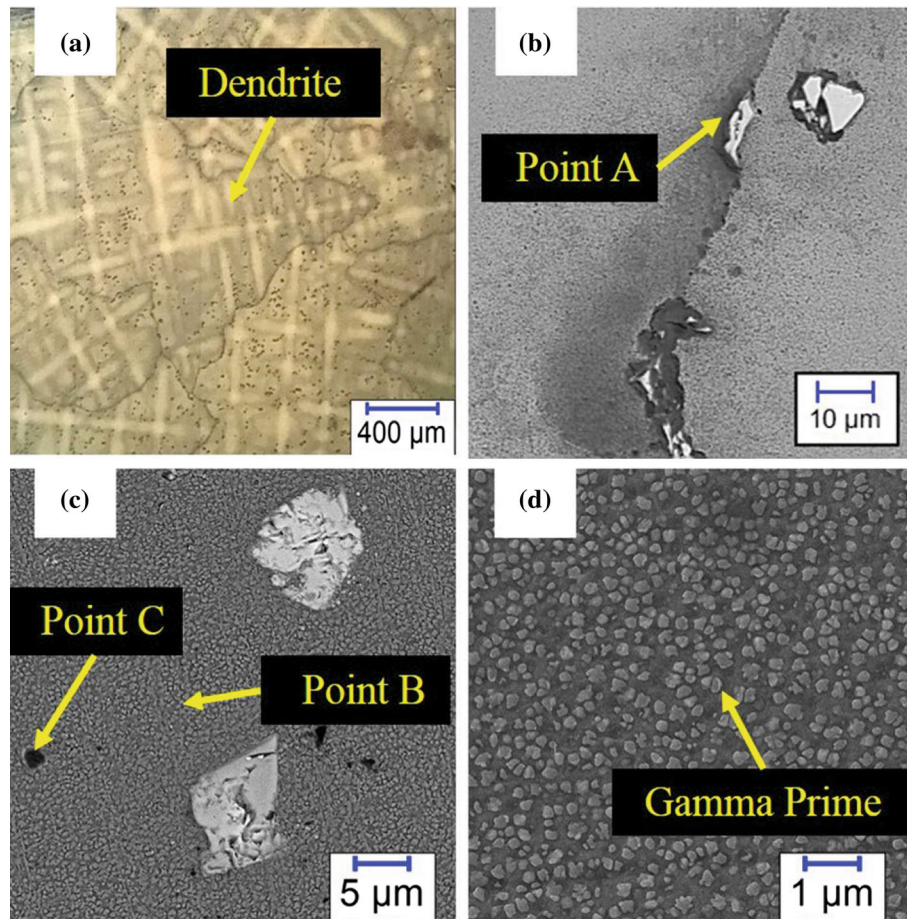


**Fig. 2** (a) Light microscope image of the base metal after hot isostatic pressing condition. FESEM images of (b) the MC carbides at grain boundaries, (c) the microstructure of the base metal, and (d) the microstructure of the base metal after heat treatment

higher temperatures (Ref 29), and thin films of  $M_{23}C_6$  Cr-rich carbides precipitate at grain boundaries. These carbides tend to form at grain boundaries with large angles and have high interfacial energy. In addition, precipitation reaction is a function of the transformation curve. Nucleation begins at low temperatures, and a discrete morphology is observed at intermediate temperature. Growth becomes important because of the continuous flow of material through the diffusion mechanism at high temperatures close to the solidus. The carbon in  $M_{23}C_6$  is distributed between the MC carbide and matrix when the temperature is above the solvus.

Figure 2(c) shows the precipitated  $\gamma'$  and  $\eta$  phases and the MC carbides in the microstructure of the base metal. Figure 2(d) illustrates the microstructure of the specimen that was heat-treated at 1160 °C for 4 h before welding. The austenitic gamma matrix contained about 30% uniformly distributed  $\gamma'$  precipitates whose diameters were about 200-300 nm and had highly disordered morphologies.

Table 3 presents the FESEM-EDS analysis of each phase that exists in Fig. 2. The three major elements in point A are Ta (15.90%), Ti (47.04%), and Nb (25.24%). Elements such as Ti, Nb, Ta, and W that was detected in the chemical analysis is known as carbides-forming elements in IN-939 and can affect the weldability of this alloy. However, owing to the difficulty of the EDS analyzer to quantify the light elements with sufficient accuracy, carbon concentration was unable to be determined. Point B contains 42.96% Ni and 22.58% Cr, which indicates a  $\gamma$  solid solution matrix. Point C is rich in Ni (6.68%) and Ti (69.64%) and shows the  $\eta$  phase (Ref 30).

### 3.2 Sigmajig Test

Figure 3 shows the micrograph of the weld zone in a Sigmajig test specimen. The HAZs of all the specimens contained grain boundary cracks. All the cracks originated from the boundary between the melting zone and the HAZ and propagated into the base metal. Figure 4 displays the radiographic images of the weld-induced cracks. The level of cracking decreased from specimens 1 to 4. However, in this method, the cracks can be detected only when propagated in a direction that produces a change in thickness parallel to the x-ray beam. Hence, the five cross-sections of the specimens were metallographically investigated, and the lengths of the cracks at the grain boundaries in the HAZ were measured.

Table 4 gives the TCL and average crack length (ACL) and the size of the HAZ (SHAZ) for each specimen. The data are given in Table 2, and the comparison of ACL and SHAZ values in Fig. 5 indicates that the average crack length is a function of the size of the HAZ.

### 3.3 Optimization

The Taguchi method was used to investigate the impact of the variables of the Sigmajig test on the TCL (Table 2). The

effectiveness of each variable was measured by using signal-to-noise ratio (S/N), which refers to the deviation of a parameter value from its optimal state. A higher S/N means that a parameter level is more favorable (Ref 31). The goal of the study was to reduce cracking; thus, the optimization logic was “Less is Better.” The formula of S/N is given in Eq 1.

$$S/N = -10 \log \left[ \frac{1}{n} \sum_{j=1}^n Y_{ij}^2 \right]. \quad (\text{Eq 1})$$

The average values of S/N for the control factors at each level are presented in Fig. 6 and Table 5. The results demonstrated that weldability is affected by flexural load with 80% impact, followed by welding speed with 9.7% impact, and heat input with 9.2% impact.

### 3.4 Microstructure

The hardness distributions given in Fig. 7 show that the hardness of the HAZ is lower than those of the weld metal and base metal. TCL was positively related to the hardness of the HAZ. The microstructure of HAZ was examined by scanning electron microscopy and variations in the elemental composition were investigated to determine the cause of this relationship. The HAZs of all the specimens were subjected to residual stress measurement.

The variations in the chemical composition of the weld metal, HAZ, and base metal as determined by EDS analysis are shown in Fig. 8. The Ti and Al contents of the HAZ greatly declined during welding, because heat generation segregates Al and Ti, which are in the solidification stage, and enhances the Al and Ti in the liquid (Ref 22). Some researchers also indicated that chemical gradients can affect  $\gamma'$  re-precipitation behavior during the welding cycle; thus, the morphology and volume fraction of different regions in this phase are necessary to compare.

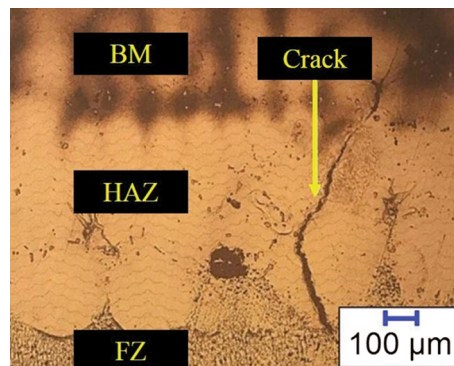


Fig. 3 Light microscope image of the weld zone

Table 3 FESEM-EDS chemical analysis (at.%) of the points indicated in Fig. 2

	Ni	Ti	Nb	Ta	W	Cr	Expected phases
Point A	0.91	47.04	25.24	15.90	1.58	0.24	MC carbide
Point B	42.96	4.70	1.47	0.67	0.97	22.58	$\gamma$ solid solution
Point C	6.68	69.64	4.19	2.2	0.75	6.44	$\eta$

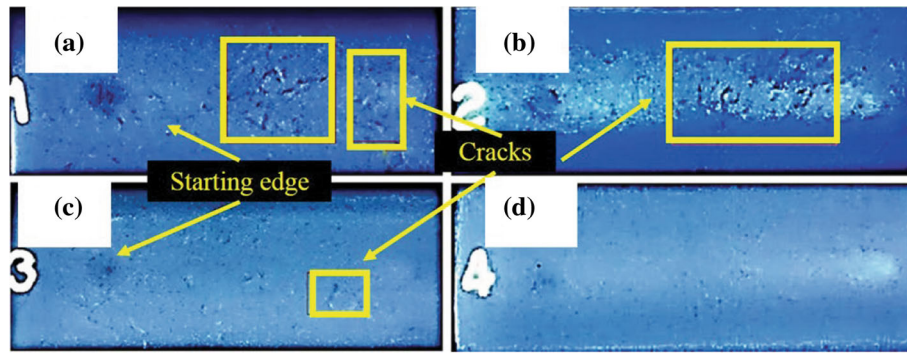


Fig. 4 Radiographic images of (a) sample 1, (b) sample 2, (c) sample 3, and (d) sample 4

Table 4 Sigmajig test conditions and the TCL, AVL, and SHAZ of each specimen

Specimen no.	Flexural load, kN	Heat input, kJ/mm	Travel speed, cm/min	TCL, $\mu\text{m}$	ACL, $\mu\text{m}$	SHAZ, $\mu\text{m}$
1	2500	2.650	18	10,943	426	400
2	2500	2.450	20	11,077	528	461
3	1250	2.650	20	1795	359	235
4	1250	2.450	18	1108	363	210

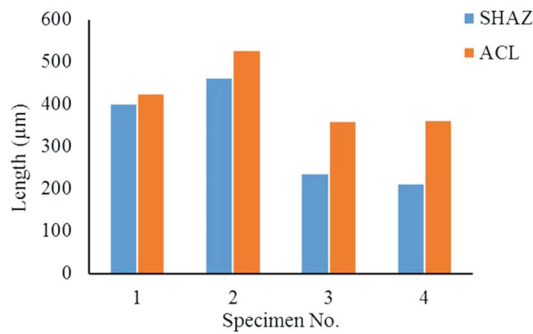


Fig. 5 Comparison of ACL and SHAZ

Figure 9 shows the morphology of the  $\gamma'$  phase in the HAZ after the Sigmajig tests of the specimens. The volume fraction of the precipitates decreased in all specimens (Table 6).

These results clearly show that the volume fraction discretion might be responsible for the sudden decline in the HAZ's hardness. Thus, the total weld-induced crack length can be associated with the hardness of the HAZ (i.e., the volume fraction of  $\gamma'$  precipitates).

Figure 10 displays an image of the weld-induced cracks that appeared in the HAZ. These grain boundary-type cracks started from the boundary between the weld metal and the HAZ and mostly grew into the base metal. Many re-melting zones were present in the vicinity of the cracks. Figure 11 displays an image of the cracks and re-melted layers at the grain

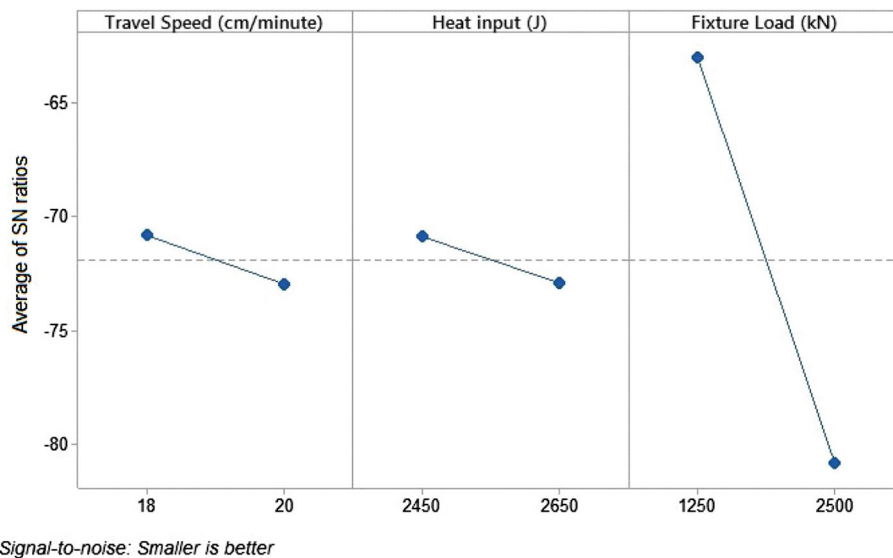
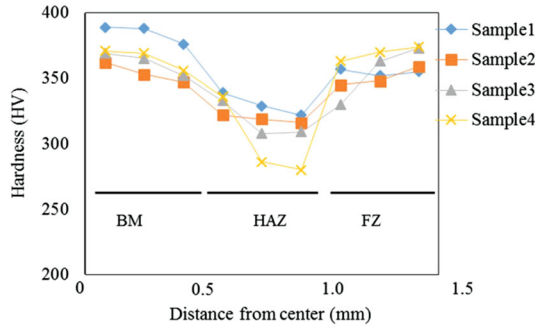


Fig. 6 Average S/N values at the considered levels

**Table 5** Response table for S/N

Level	Flexural load, kN	Heat input, kJ/mm	Travel speed, cm/min
1	– 62.99	– 70.89	– 70.84
2	– 80.84	– 72.93	– 72.98
Delta	17.85	2.04	2.15
Rank	1	3	2
%	81.1	9.2	9.7



**Fig. 7** Hardness plot of the specimens

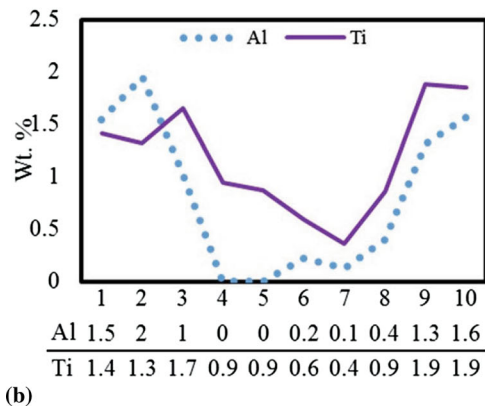
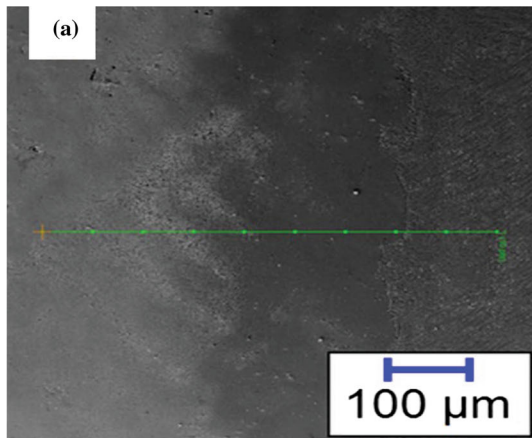


**Fig. 8** EDS analysis of the chemical composition of the weld metal, HAZ, and base metal

boundaries. The cause of the crack nucleation seems to be the melted layer.

According to the elemental analysis of point A, Ta, Ti, and C accounted for about 90 wt.%, which indicates the existence of MC carbide. The results of the elemental analysis of point B in the melted layer and point C in the base metal are presented in Fig. 12(a) and (b), respectively. The melted area contained Ni, C, Cr, and Co, which show the co-existence of  $M_{23}C_6$  carbide and  $\gamma$  phase. A sharp decrease in the Al and Ti contents (from 3.97 to 2.87) and a 10% increase in Cr content were observed from the base metal to the melted layer. This depletion of the grain boundary from the major constituents of the  $\gamma'$  phase can be explained by the reversible reaction given in Eq 2 (Ref 24). According to the reaction,  $M_{23}C_6$  carbides precipitate within the grain boundaries, and  $\gamma'$  precipitates deposit around these boundaries. The difference between the crystalline lattice of  $\gamma'$  precipitates and the matrix creates local residual stresses that weaken the grain boundaries and facilitate grain boundary cracking.



The magnified image in Fig. 13 shows that the cause of crack nucleation is the re-melting of the adjacent area. Besides, the presence of eutectic melting zones, such as  $\gamma$ - $\gamma'$  eutectic, can cause crack nucleation.

The cracking in the HAZ directly resulted from a reaction between intergranular liquation and mechanical driving force because of the tensile stresses created during welding. Miller et al. proposed Eq 3 (Ref 32), which is related to grain boundary cracking in the melted layers of other alloys. This equation defined the tension needed to prevail surface tension  $\gamma_{SL}$  on a grain boundary containing liquid film of thickness  $h$ :

$$\sigma = 2\gamma_{SL}/h, \quad (\text{Eq 3})$$

where  $\sigma$  is the stress required for separation and cracking,  $\gamma_{SL}$  is the interface energy, and  $h$  is the thickness of the melted layer. According to this equation, weld metal with poor stress relaxation was suitable for grain boundary cracking. Also, the results of the hardness tests (Fig. 8) and crack length measurements (Fig. 6) clearly showed that the specimens with harder HAZ contained more cracks. Therefore, a residual stress test was performed on the samples to know the relationship between the hardness of the HAZ zone and stress relaxation.

### 3.5 Residual Stresses Measurement

Residual stresses and distortions are unavoidable in welding. XRD is an established technique for measuring residual stress. We discussed in detail the complete method for measuring and calculating residual stresses in this work. The XRD measurements of residual stresses near the weld bead are based on Eq 4:

$$\sigma_\phi = \frac{E}{(1+\nu)d_0} \left( \frac{d\phi\psi - d_0}{\sin^2\psi} \right), \quad (\text{Eq 4})$$

where  $\sigma_\phi$  is the surface residual stress,  $d_0$  is the stress-free spacing of the  $(hkl)$  lattice planes,  $E$  is Young's modulus, and  $\nu$  is Poisson's ratio. According to Rai (Ref 25), the  $\left( \frac{d\phi\psi - d_0}{\sin^2\psi} \right)$  in Eq 4 is the slope, which can be calculated from the plot of  $d$  measured at various  $\psi$  angles with  $\sin^2\psi$ . Therefore, Eq 4 can be further modified to calculate stress as shown in Eq 5:

$$\sigma_\phi = \frac{m}{d_0} \left[ \frac{E}{1+\nu} \right]. \quad (\text{Eq 5})$$

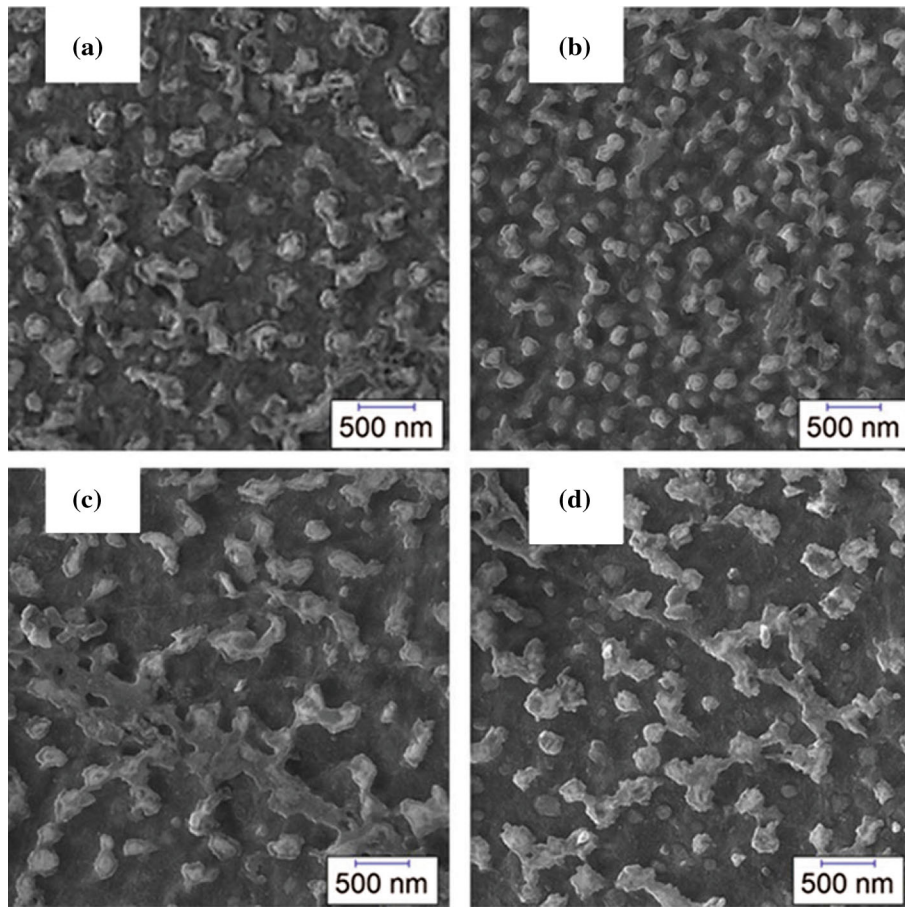


**Fig. 9** FESEM images of the  $\gamma'$  phase in the HAZs of (a) sample 1, (b) sample 2, (c) sample 3, and (d) sample 4

**Table 6** Comparison of volume fraction of  $\gamma'$  precipitates and hardness in HAZ

Specimen no.	1	2	3	4	Base metal
$\gamma'$ phase, %	24	26	22	16	37
Hardness, HV	321 $\pm$ 1	330 $\pm$ 6	313 $\pm$ 6	294 $\pm$ 15	389 $\pm$ 10

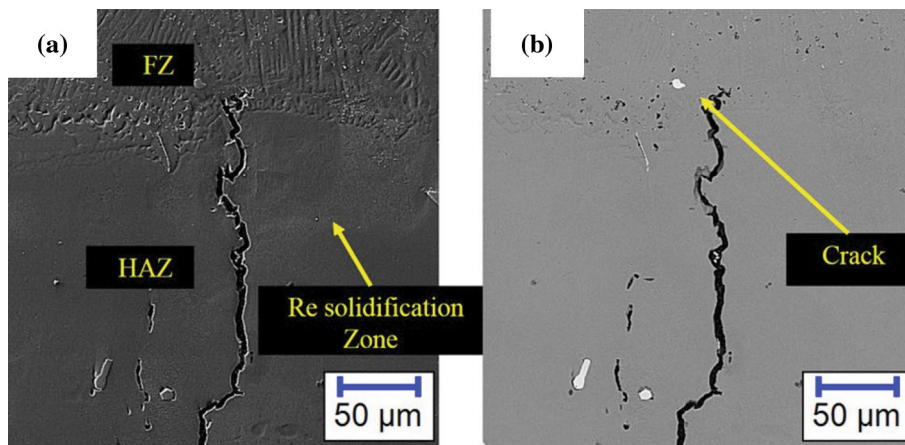


**Fig. 10** (a) SE and (b) BSE FESEM images of the cracks that appeared in the HAZ

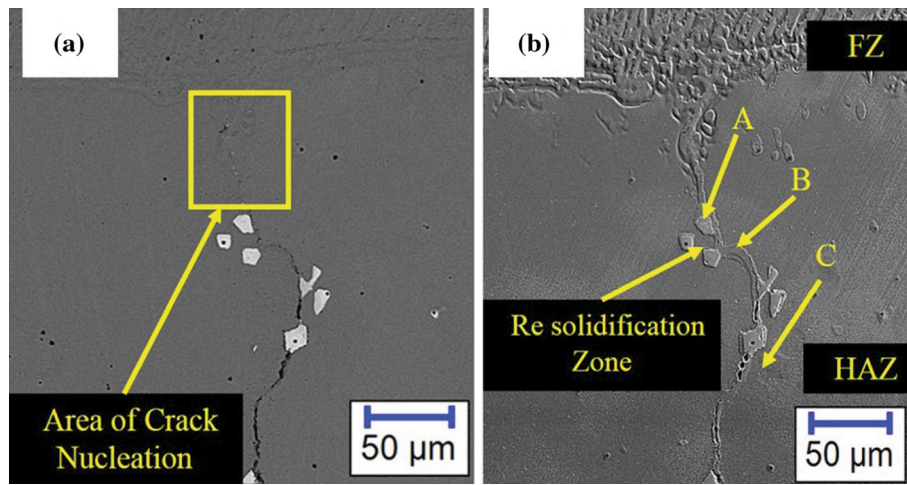


**Fig. 11** (a) SE and (b) BSE FESEM images of the cracks and re-melting areas in the HAZ

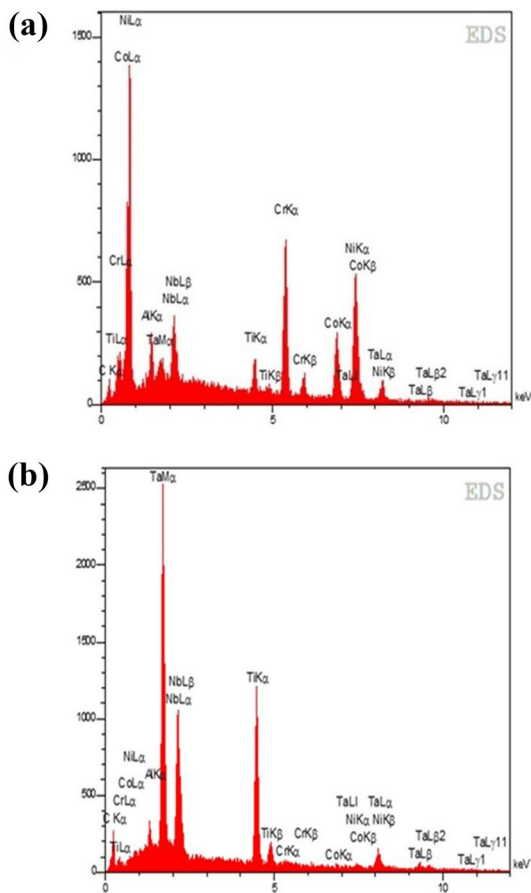


**Fig. 12** EDS spectra of the (a) re-melted layer and (b) base metal

Therefore, the residual stresses can be determined from known variables ( $E$ ,  $d_0$ , and  $\nu$ ) and the slope  $m$ . The peak shift at various angles (ranging from  $0^\circ$  to  $33^\circ$  with steps of  $1.3^\circ$ ) and  $d$ -spacing relationships were used for estimating the residual stresses. Then, the  $\sin^2\psi$  versus  $d$ -spacing plot for all four specimens is given in Fig. 14.

Table 7 depicts residual stresses calculated for each sample. The existence of residual stresses is a very important factor in cracking. Any factor that contributes to stress will also cause

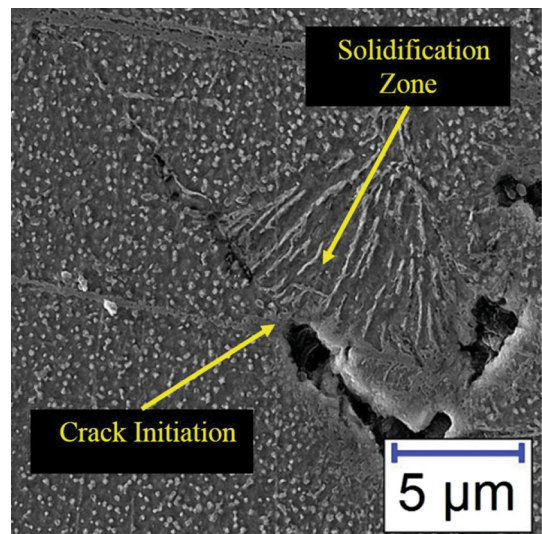


**Fig. 13** FESEM image of the cracks in the HAZ

cracking. Thus, increased flexural load, heat input, and welding speed will cause cracking.

The outcomes of the hardness tests and metallographic investigations indicated that the total length of welding-induced cracks increased dramatically with increased HAZ hardness. In addition, the comparison of the residual stress and hardness test results showed that a low-hardening base alloy, which has the potential to relieve substantial stresses, can decrease the moving force of intergranular liquation cracking. Thus, the resistance to cracking will increase by reducing the hardness of the HAZ.

#### 4. Conclusions

The effects of welding parameters on intergranular liquation cracking formation, mechanical properties, and residual stress generation during the repair welding of IN-939 were investigated. The following conclusions can be drawn from this study:

1. The results of the metallographic investigations indicated that the microstructure of IN-939 is very susceptible to



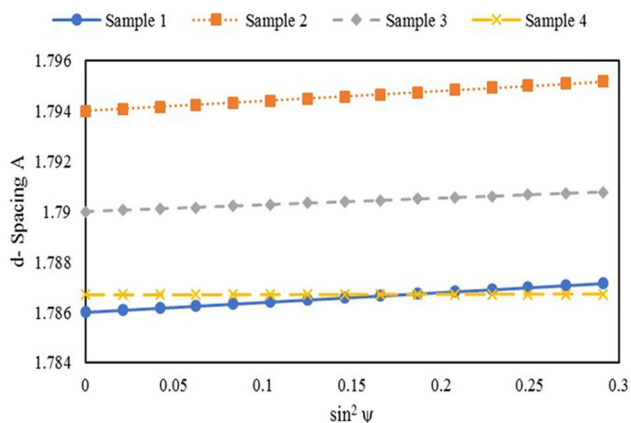


Fig. 14  $d_0 - \sin^2\psi$  diagrams of samples

Table 7 Residual stresses of each sample

Sample no.	$E$ , GPa	$\nu$	$d_0$ , Å	$m$ , Å	$\sigma_\phi$ , MPa
1	165	0.3	1.7860	0.00394	280
2	165	0.3	1.7941	0.00400	283
3	165	0.3	1.7880	0.00267	189
4	165	0.3	1.7867	0.00082	58

cracking during welding. All cracks originated from the HAZ and grew into other areas along grain boundaries. The melted zones were also in the vicinity of the cracks. The results of the elemental analysis of the melted layer showed that the melted area contains Ni, C, Cr, and Co, which show the co-existence of  $M_{23}C_6$  carbide and the  $\gamma$  phase.

- A sudden decline in hardness was observed in the HAZs because of the reduction in the volume fraction of  $\gamma'$  precipitates. A strong correlation exists between the TCL and the hardness of the HAZ. The total length of welding-induced cracks went up dramatically with the increase in the hardness of the HAZ.
- Residual stress measurement indicated that the mechanical driving force of tensile stresses during welding has a substantial effect on grain boundary cracking in the melted layers. The outcomes of the hardness tests and residual stress measurement investigations indicated that the residual stress of welding went up dramatically with the increase in the hardness of the HAZ.
- The Taguchi method analysis showed that the cracking of IN-939 during welding is affected by flexural load (81.1% impact), welding speed (9.7% impact), and heat input (9.2% impact).

## References

- A. Doroudi, A. Dastgheib, and H. Omidvar, The Bonding Temperature Effect of the Diffusion Brazing Inconel 625 Superalloy on the Microstructure Changes, Corrosion Resistance, and Mechanical Properties, *J. Manuf. Process.*, 2020, **53**, p 213–222
- A.E. Pilehrood, H. Omidvar, A. Shamsipur, and M. Khakian-Ghomi, Effect of Transient Liquid Phase Bonding Followed by Homogeniza-

- tion on the Microstructure and Hot Tensile Behavior of Inconel 738 Superalloy, *J. Manuf. Process.*, 2019, **48**, p 110–118
- C.H. William, T. Chester, and S.S. Norman, *Superalloys 2: High-Temperature Materials for Aerospace and Industrial Power*, Wiley, Hoboken, 1987
- D. Furrer and H. Fecht, Ni-Based Superalloys for Turbine Discs, *JOM*, 1999, **51**(1), p 14–17
- N. Gladys and V. Laura, Analysis of Rotor-Blade Failure Due to High-Temperature Corrosion/Erosion, *Surf. Coatings Technol.*, 1999, **120**, p 145–150
- S. Kamal, R. Jayaganthan, and S. Prakash, High Temperature Cyclic Oxidation and Hot Corrosion Behaviours of Superalloys at 900 C, *Bull. Mater. Sci.*, 2010, **33**(3), p 299–306
- A.E. Pilehrood, H. Omidvar, A. Shamsipur, and Z. Sajuri, Influence of Transient Liquid Phase Bonding Followed by Homogenization on the Fatigue Lifetimes of Inconel 738 at Elevated Temperature, *J. Manuf. Process.*, 2020, **55**, p 348–358
- M.R. Winstone, K.M. Nikbin, and G.A. Webster, Modes of Failure under Creep/Fatigue Loading of a Nickel-Based Superalloy, *J. Mater. Sci.*, 1985, **20**(7), p 2471–2476
- Z. Mazur, A. Luna-Ramírez, J.A. Juárez-Islas, and A. Campos-Amezcu, Failure Analysis of a Gas Turbine Blade Made of Inconel 738LC Alloy, *Eng. Fail. Anal.*, 2005, **12**(3), p 474–486
- D.Y. Kim, J.H. Hwang, K.S. Kim, and J.G. Youn, A Study on Fusion Repair Process for a Precipitation Hardened IN738 Ni-Based Superalloy, *J. Eng. Gas Turbines Power*, 2000, **122**(3), p 457–461
- M.J. Donachie and S.J. Donachie, *SUPERALLOYS*, 2nd ed., America, 2002
- O.A. Ojo, N.L. Richards, and M.C. Chaturvedi, Study of the Fusion Zone and Heat-Affected Zone Microstructures in Tungsten Inert Gas-Welded INCONEL 738LC Superalloy, *Metall. Mater. Trans. A*, 2006, **37**(2), p 421–433
- O.A. Ojo and M.C. Chaturvedi, Liquefaction Microfissuring in the Weld Heat-Affected Zone of an Overaged Precipitation-Hardened Nickel-Base Superalloy, *Metall. Mater. Trans. A*, 2007, **38**(2), p 356–369
- O.A. Ojo, N.L. Richards, and M.C. Chaturvedi, Contribution of Constitutional Liquefaction of Gamma Prime Precipitate to Weld HAZ Cracking of Cast Inconel 738 Superalloy, *Scr. Mater.*, 2004, **50**(5), p 641–646
- M.A. González, D.I. Martínez, A. Pérez, H. Guajardo, and A. Garza, Microstructural Response to Heat Affected Zone Cracking of Prewelding Heat-Treated Inconel 939 Superalloy, *Mater. Charact.*, 2011, **62**(12), p 1116–1123
- B. Jahnke, High-Temperature Electron Beam Welding of the Nickel-Base Superalloy IN-738 LC, *Weld. J. Res. Suppl.*, 1982, **61**
- R. Thamburaj, W. Wallace, and J.A. Goldak, Post-Weld Heat-Treatment Cracking in Superalloys, *Int. Met. Rev.*, 1983, **28**(1), p 1–22
- O.A. Ojo and M.C. Chaturvedi, On the Role of Liquefied  $\Gamma'$  Precipitates in Weld Heat Affected Zone Microfissuring of a Nickel-Based Superalloy, *Mater. Sci. Eng. A*, 2005, **403**(1–2), p 77–86
- S.W.K. Shaw and others, Response of IN-939 to Process Variations, *Superalloys 1980*, The Minerals, Metals & Materials Society, 1980, p 275–284
- Z. Miskovic, Of IN 939 Superalloy, 1992, p 709–711
- M.A. González-Albarrán, D.I. Martínez, E. Díaz, J.C. Díaz, I. Guzman, E. Saucedo, and A.M. Guzman, Effect of Preweld Heat Treatment on the Microstructure of Heat-Affected Zone (HAZ) and Weldability of Inconel 939 Superalloy, *J. Mater. Eng. Perform.*, 2014, **23**(4), p 1125–1130
- M. Tajally, A Study on Microstructure and Phase Transformation in the Weld Fusion Zone of TIG-Welded IN939 with IN625 and IN718 as Filler Metal, *Metall. Mater. Trans. A*, 2020
- I. Guzman, E. Saucedo, M.A. Gonza, and M.A. Gonza, Effect of Preweld Heat Treatment on the Microstructure of Heat-Affected Zone (HAZ) and Weldability of Inconel, *J. Mater. Eng. Perform.*, 2014, **23**, p 1125–1130
- F. Jafarian, H. Amirabadi, and J. Sadri, Experimental Measurement and Optimization of Tensile Residual Stress in Turning Process of Inconel718 Superalloy, *Measurement*, 2014, **63**, p 1–10
- B. Raj, T. Jayakumar, S. Mahadevan, and S.K. Rai, X-Ray Diffraction Based Residual Stress Measurements for Assessment of Fatigue Damage and Rejuvenation Process for Undercarriages of Aircrafts, *J. Nondestruct. Eval.*, 2009, **28**(3–4), p 157

26. D.A. Lesyk, S. Martinez, B.N. Mordiyuk, V.V. Dzhemelinskyi, A. Lamikiz, and G.I. Prokopenko, Post-Processing of the Inconel 718 Alloy Parts Fabricated by Selective Laser Melting: Effects of Mechanical Surface Treatments on Surface Topography, Porosity, Hardness and Residual Stress, *Surf. Coatings Technol.*, 2020, **381**, p 125136
27. Q. Luo and A.H. Jones, Surface & Coatings Technology High-Precision Determination of Residual Stress of Polycrystalline Coatings Using Optimised XRD-Sin  $2\psi$  Technique, *Surf. Coat. Technol.*, 2010, **205**(5), p 1403–1408
28. J. Andersson, Weldability of Precipitation Hardening Superalloys—Influence of Microstructure, Chalmers University of Technology, 2011
29. G. Lvov, V.I. Levit, and M.J. Kaufman, Mechanism of Primary MC Carbide Decomposition in Ni-Base Superalloys, *Metall. Mater. Trans. A*, 2004, **35**(6), p 1669–1679
30. M.R. Jahangiri, H. Arabi, and S.M.A. Boutorabi, Investigation on the Dissolution of  $\eta$  Phase in a Cast Ni-Based Superalloy, *Int. J. Miner. Metall. Mater.*, 2013, **20**(1), p 42–48
31. M.R. Akbarpour, A. Mashhuriazar, and M. Daryani, Experimental and Numerical Investigation on the Effect of the Tempcore Process Parameters on Microstructural Evolution and Mechanical Properties of Dual-Phase Steel Reinforcing Rebars, *Met. Mater. Int.*, 2020, p 1–10
32. W.A. Miller and G.A. Chadwick, On the Magnitude of the Solid/Liquid Interfacial Energy of Pure Metals and Its Relation to Grain Boundary Melting, *Acta Metall.*, 1967, **15**(4), p 607–614

**Publisher's Note** Springer Nature remains neutral with regard to jurisdictional claims in published maps and institutional affiliations.